Supplementary Information to "Dilatancy, shear jamming, and a generalized jamming phase diagram of frictionless sphere packings"

Varghese Babu,[1,*] Deng Pan,[2,*] Yuliang Jin,[2,3,†] Bulbul Chakraborty,[4] and Srikanth Sastry[1,‡]

[1] *Jawaharlal Nehru Centre for Advanced Scientific Research, Jakkur Campus, Bengaluru 560064, India.*
[2] *CAS Key Laboratory of Theoretical Physics, Institute of Theoretical Physics, Chinese Academy of Sciences, Beijing 100190, China*
[3] *School of Physical Sciences, University of Chinese Academy of Sciences, Beijing 100049, China*
[4] *Martin Fisher School of Physics, Brandeis University, Waltham, MA 02454, USA.*

S1. MODELS

The two models represent systems that consist of $N = 2000$ (unless otherwise specified) bi-disperse (BD) and poly-disperse (PD) spheres. The bi-disperse system consists of N equal-mass spheres with a diameter ratio $D_1/D_2 = 1.4$ and a number ratio $N_1/N_2 = 1$. The PD system contains N equal-mass spheres whose diameter distribution is characterized by $P(D) \sim D^{-3}$, for $D_{\min} \leq D \leq D_{\min}/0.45$. In both the BD and the PD models, the particles interact via a purely-repulsive, harmonic potential, $v_{ij}(r) = \frac{1}{2}(1 - r/D_{ij})^2$ (zero if $r > D_{ij}$), where r is the inter-particle distance and $D_{ij} = (D_i + D_j)/2$, is the just-touching distance between particles i and j. The volume fraction is $\phi = \rho(1/6)\pi\overline{D^3}$, where ρ is the number density N/V, and V is the volume of simulation box.

S2. SIMULATION DETAILS

A. Constant volume athermal quasi-static shear

(i) In the BD model, constant volume athermal quasistatic shear (AQS) simulations are carried out using LAMMPS[1]. To simulate a uniform simple shear deformation, at each step an affine transformation is applied to the position of each particle, $x' = x + \delta\gamma \times z, y' = y, z' = z$, where $\delta\gamma = 10^{-4}$, followed by energy minimization using the conjugate gradient (CG) method. The CG procedure stops when the maximum component of the force vector is less than 10^{-16}. The energy minimization stops when the maximum distance moved by any particle is less than the machine precision during an iteration. The norm of the equilibrium net force vector is of the order of 10^{-13} and the maximum component is of the order of 10^{-14} at the termination of minimization.

(ii) In the PD model, the affine transformation is applied with the same step size $\delta\gamma = 10^{-4}$, followed by energy minimization using the FIRE algorithm [2]. The minimization procedure stops when the percentage of force balanced particles with net force magnitude $|f| \leq 10^{-14}$ reaches 99.5%.

B. Constant pressure athermal quasistatic shear

In constant pressure AQS simulations, the energy minimization is replaced by the minimization of enthalpy $H = U + PV$ at the imposed pressure P. (i) In the BD model, the minimization stops when the maximum distance moved by any particle during a minimization step is less than the machine precision. (ii) In the PD model, the minimization stops if the percentage of force balanced particles reaches 99.5%, and the deviation from the target pressure is less than 10^{-4}.

C. Protocols to prepare initial configurations

(i) Mechanical annealing by cyclic AQS for the BD model. We first use the method in [3] to generate packings with jamming density $\phi_J \approx 0.648$. The initial configurations are hard-sphere (HS) configurations at a packing

* These authors contributed equally.
† yuliangjin@mail.itp.ac.cn
‡ sastry@jncasr.ac.in

fraction of $\phi = 0.363$, which are equilibrated using the Monte-Carlo (MC) algorithm. We switch to the harmonic soft-sphere potential, rapidly compress the configurations by rescaling the volume of the simulation box (till $\beta P/\rho$ decays to ~ 1000, where β is the inverse temperature), and remove the resulting overlaps by using MC simulations. The temperature is then switched off, and the system is further quasistatically compressed, by inflating the particles uniformly, followed by energy minimization using the CG method. The compression stops when the energy per particle $e = E/N$, after minimization, remains above 10^{-16}. This is used as the criterion for jamming. Then the system is slowly decompressed till $e < 10^{-16}$, which generates configurations corresponding to jamming density $\phi_J \approx 0.648$.

We then use mechanical annealing to increase the jamming density from ϕ_J to $\phi_j > \phi_J$. The configurations obtained from the above procedure are compressed to various over-jamming densities $\phi > \phi_J$, and are unjammed using cyclic AQS, $\gamma = 0 \to \gamma_{max} \to 0 \to -\gamma_{max} \to 0$, where the strain amplitude $\gamma_{max} = 0.07$ [4], and the strain step $\delta\gamma = 10^{-3}$. These configurations correspond to jamming densities $\phi_j > \phi_J$. See FIG S12 for the dependence of ϕ_j on protocol parameters.

(ii) Thermal annealing by a swap algorithm for the PD model. We first prepare dense equilibrium HS configurations at ϕ_g, using the the swap algorithm [5]. At each swap MC step, we exchange the positions of two randomly picked particles as long as they do not overlap with other particles. Combined with standard event-driven molecular dynamics (MD), such non-local swap moves significantly speed up the equilibration procedure. The poly-dispersity of the model suppresses crystallization even in deep annealing, and optimizes the efficiency of the algorithm [5].

For each equilibrium configuration at ϕ_g, we then perform a rapid quench to generate the jammed configuration at ϕ_j (see Ref. [6] for the relationship between ϕ_g and ϕ_j). In particular, the J-point state at $\phi_J \simeq 0.655$ are quenched from random initial configurations with $\phi_g = 0$ [7]. The rapid quench is realized by inflating the particle sizes instantaneously to reach the target density, switching to the harmonic soft-sphere potential, and then minimizing the total potential energy using the FIRE algorithm [2]. The same jamming criterion is used as in the BD model.

D. Calculation of the stress tensor and the pressure

The stress tensor is calculated using the formula,

$$\hat{\sigma} = -\frac{1}{V}\sum_{i<j} \vec{f}_{ij} \otimes \vec{r}_{ij}, \tag{S1}$$

where $\vec{f}_{ij}$ and $\vec{r}_{ij}$ are the inter-particle force and distance vectors between particles i and j. The pressure P is related to the trace of the stress tensor, $P = -(\sigma_{xx} + \sigma_{yy} + \sigma_{zz})/3$, which can be written as,

$$P = \frac{1}{3V}\sum_{i<j} \vec{f}_{ij} \cdot \vec{r}_{ij}. \tag{S2}$$

S3. ADDITIONAL DATA FOR SHEAR JAMMING

The unjammed configurations at a density ϕ, where $\phi_J < \phi < \phi_j$, undergo shear jamming when subjected to steady shear at constant volume. Shear jamming can be detected by a sharp increase in the stress σ_{xz} and in the coordination number Z_{NR} with increasing strain, as shown in Fig. 1. Additionally, FIG S1 shows how the pressure P and the potential energy PE increase with strain. In the mechanical annealing protocol, the shear jamming strain γ_j, which is indicated by an abrupt jump of the pressure P in FIG S2, is always greater than $\gamma_{max} = 0.07$, the training amplitude used in the cyclic shearing.

We also calculate the macroscopic friction $\mu = \sigma_{xz}/P$ of the configurations as a function of $\gamma - \gamma_j$ (FIG S3), which shows a peak in the cases when there is a significant overshoot in the stress-strain curve (Fig. 1). This peak, appearing after the shear jamming strain γ_j, also exists in the uniform shear of over-compressed systems (FIG S4). In both cases, the peak occurs near the yielding point.

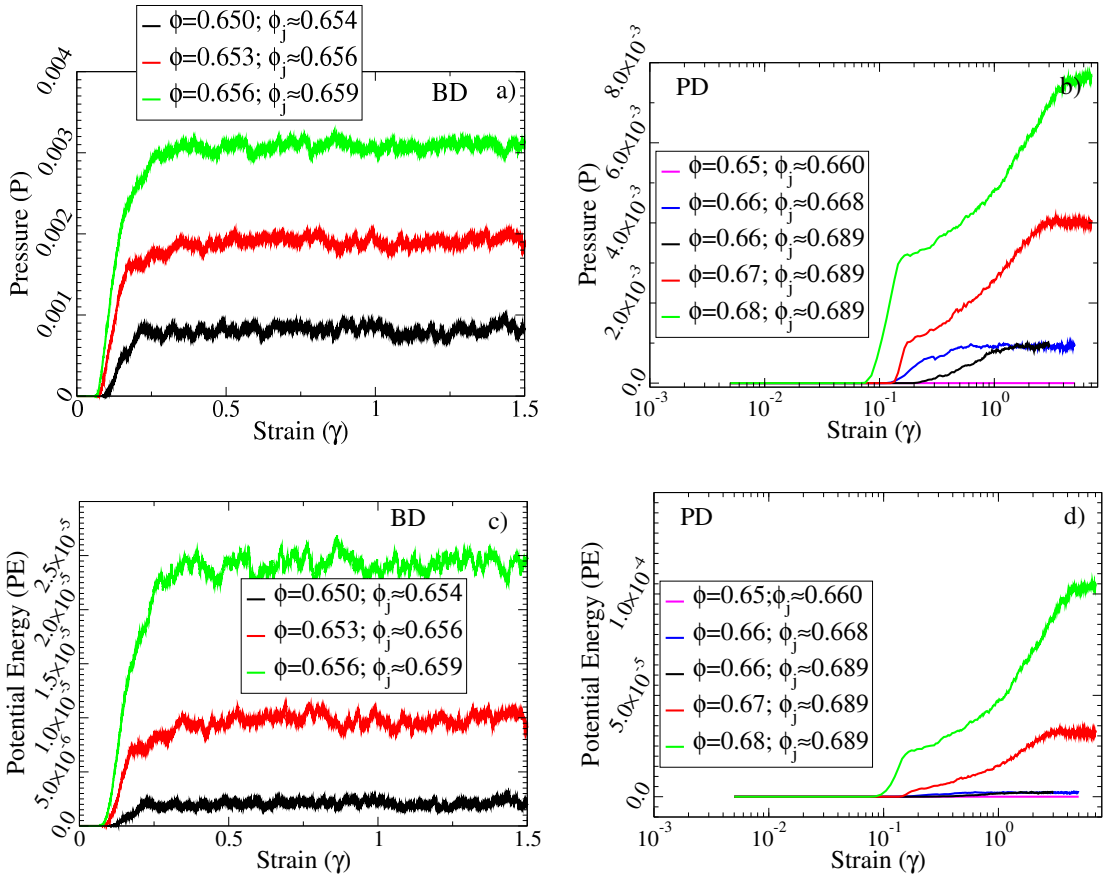

FIG. S1. **Evolutions of a-b) pressure P and c-d) potential energy PE with strain γ during shear jamming.** The constant volume uniform AQS is applied. Data are presented for a few different ϕ and ϕ_j, obtained in both BD and PD systems.

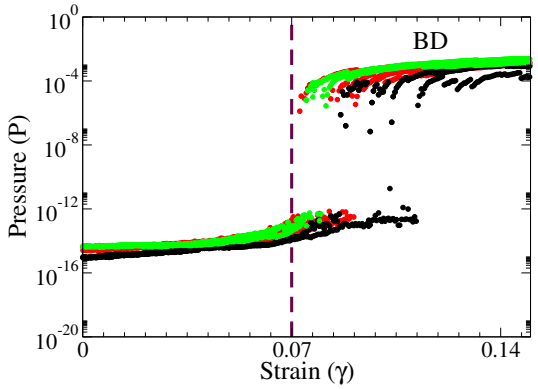

FIG. S2. **Shear jamming under uniform shear in mechanically annealed BD systems.** The pressure increases abruptly as the system is strained beyond $\gamma = \gamma_{max}$, indicating shear jamming. We present multiple realizations for each ϕ_j, where $\phi_j = 0.659$ (green), 0.656 (red), and 0.654 (black). The densities at which shear is carried out are $\phi = 0.656$ (green), 0.653 (red), and 0.650 (black).

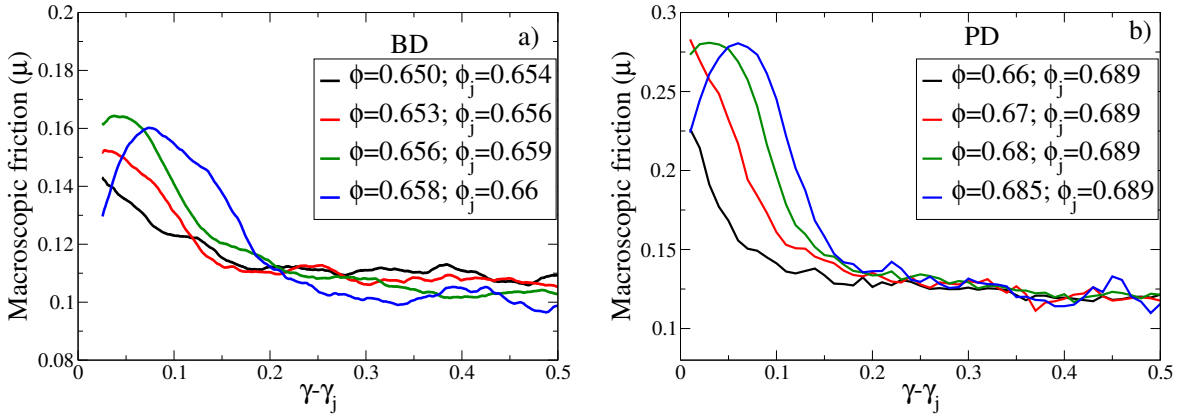

FIG. S3. **Macroscopic friction μ as a function of distance from jamming strain $\gamma - \gamma_j$ for a) BD and b) PD systems.** The jamming strain γ_j is identified as the strain at which σ_{xz} increases above 10^{-11} in BD systems, and above 10^{-8} in PD systems.

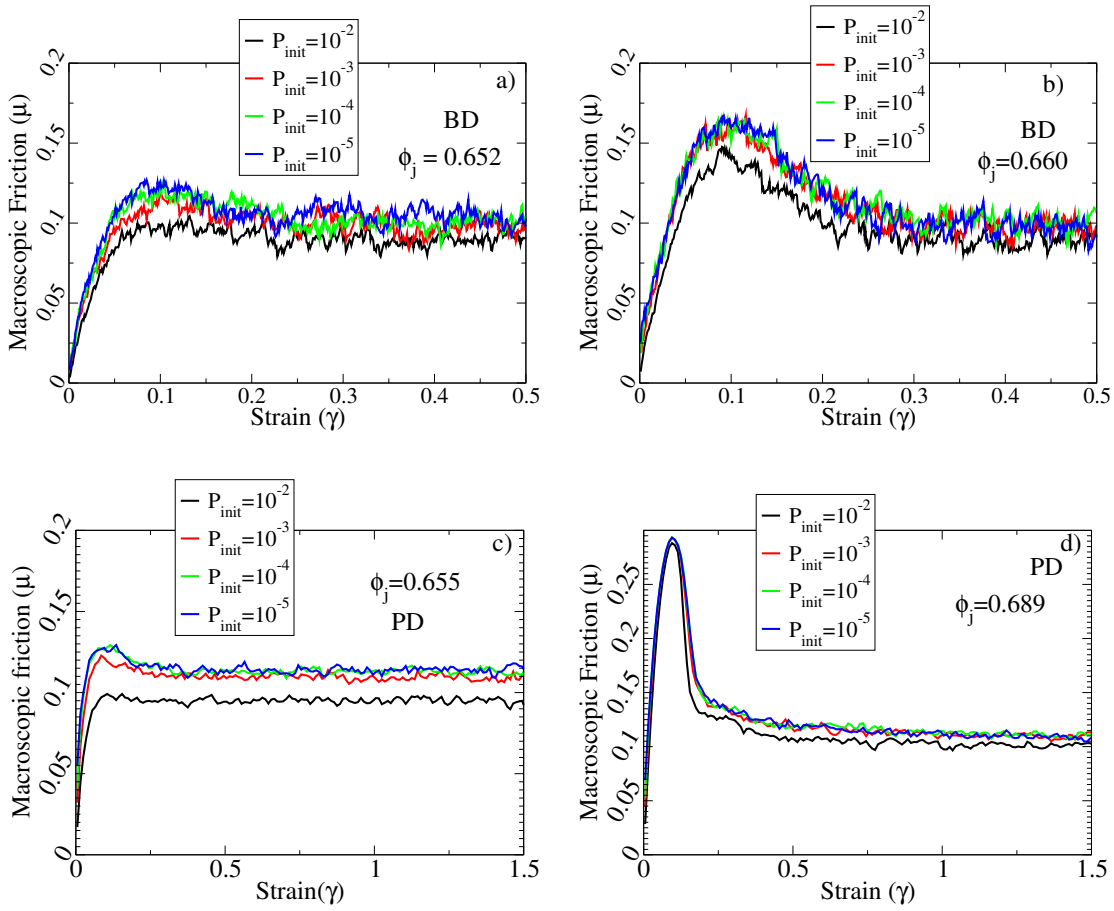

FIG. S4. **Microscopic friction μ of over-compressed systems ($P_{init} > 0$, $\phi > \phi_j$) as a function of strain γ under constant volume shear.** Data are plotted for two different ϕ_j and four different P_{init} in both BD and PD models.

S4. ADDITIONAL DATA FOR THE DILATANCY EFFECT UNDER CONSTANT PRESSURE SHEAR

Figure S5 shows that, under constant pressure shear deformations, the degree of dilation $\delta\phi = \phi_{init} - \phi_s$, which is the difference between the initial density ϕ_{init} and the steady-state density ϕ_s, increases with the jamming density ϕ_j for a fixed pressure P, or decreases with P for a fixed ϕ_j.

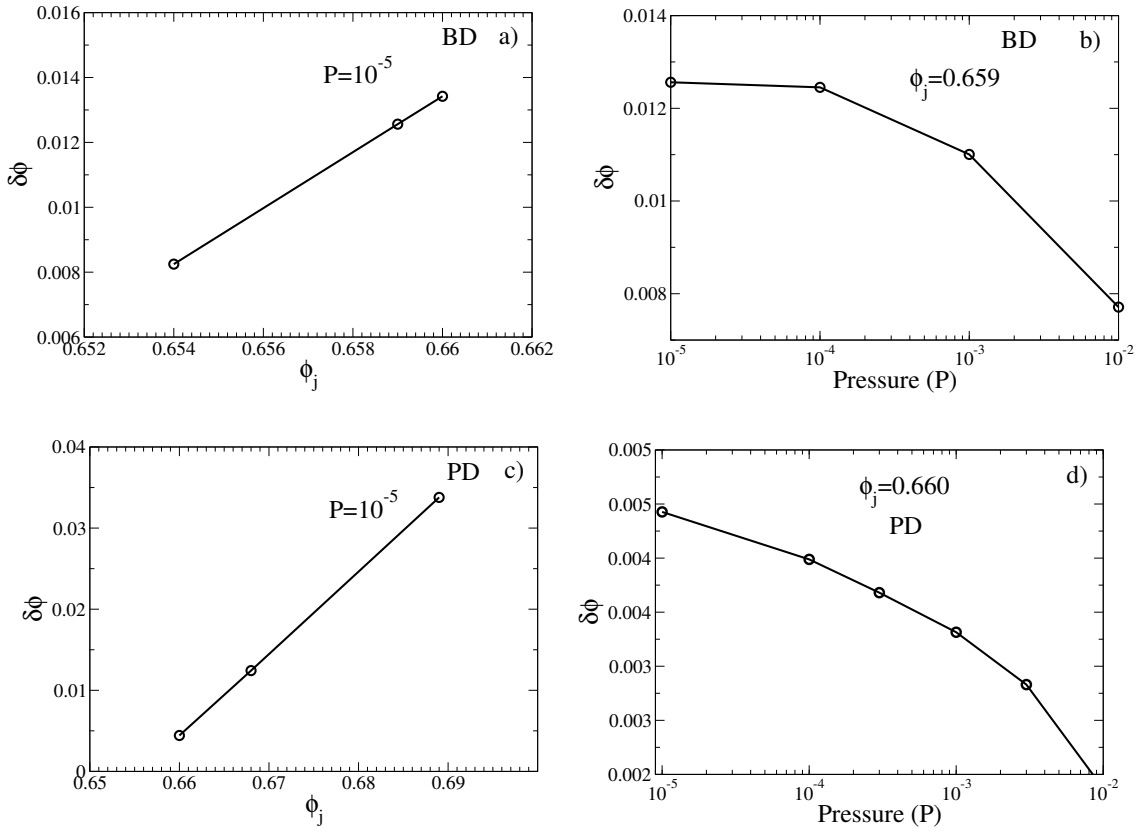

FIG. S5. **Degree of dilation in constant pressure shear deformations. a) and c)** Degree of dilation $\delta\phi$ as a function of ϕ_j for a given pressure P, and **b) and d)** as a function of P for a given ϕ_j.

S5. FINITE SIZE ANALYSIS OF THE J-POINT DENSITY ϕ_J AND CRITICAL STATE DENSITY ϕ_c

BD model. The jamming density ϕ_J is identified using multiple cycles of compressions and decompression follows. Starting from the randomly initialized configuration, the system is compressed in steps of $\delta\phi = 5 \times 10^{-4}$ till energy per particle is above 10^{-6}. Here the jamming density has been crossed. Then $\delta\phi$ is divided by 2 and the configuration is decompressed till system is unjammed. A system is considered unjammed if the energy per particle is less than 10^{-16}. This cycle is repeated till $\delta\phi < 10^{-6}$ and the jamming density is identified during the decompression.

These configurations at the jamming density are compressed to various finite pressures $P = P_s$ and sheared using constant pressure AQS. The steady state packing fraction $\phi_s(P_s)$ is measured and ϕ_c is estimated by fitting the data with linear relation $P_s \sim \phi_s - \phi_c$.

We average over a number of configurations to calculate ϕ_c and ϕ_J, for $N = 250, 500, 1000, 2000, 4000$. For ϕ_c, we have used 72,56,10,10,10 configurations respectively, and for ϕ_J we have used 500,500,500,100,100 configurations.

PD model. Our analysis is based on simulation data obtained from systems that consist of $N = 250$, 500, 1000, 2000, 4000 particles, with 256, 192, 128, 64, 64, 64 independent samples respectively.

To estimate the J-point density ϕ_J, we follow the procedure employed in Ref [8]: starting from a random initial configuration, the system is compressed and decompressed iteratively, followed with energy minimization after each step, until reaching the jamming/unjamming threshold where the energy is infinitesimally positive. More specifically, the particles are inflated instantly to increase the volume fraction by $\delta\phi = 5 \times 10^{-4}$ during each compression step.

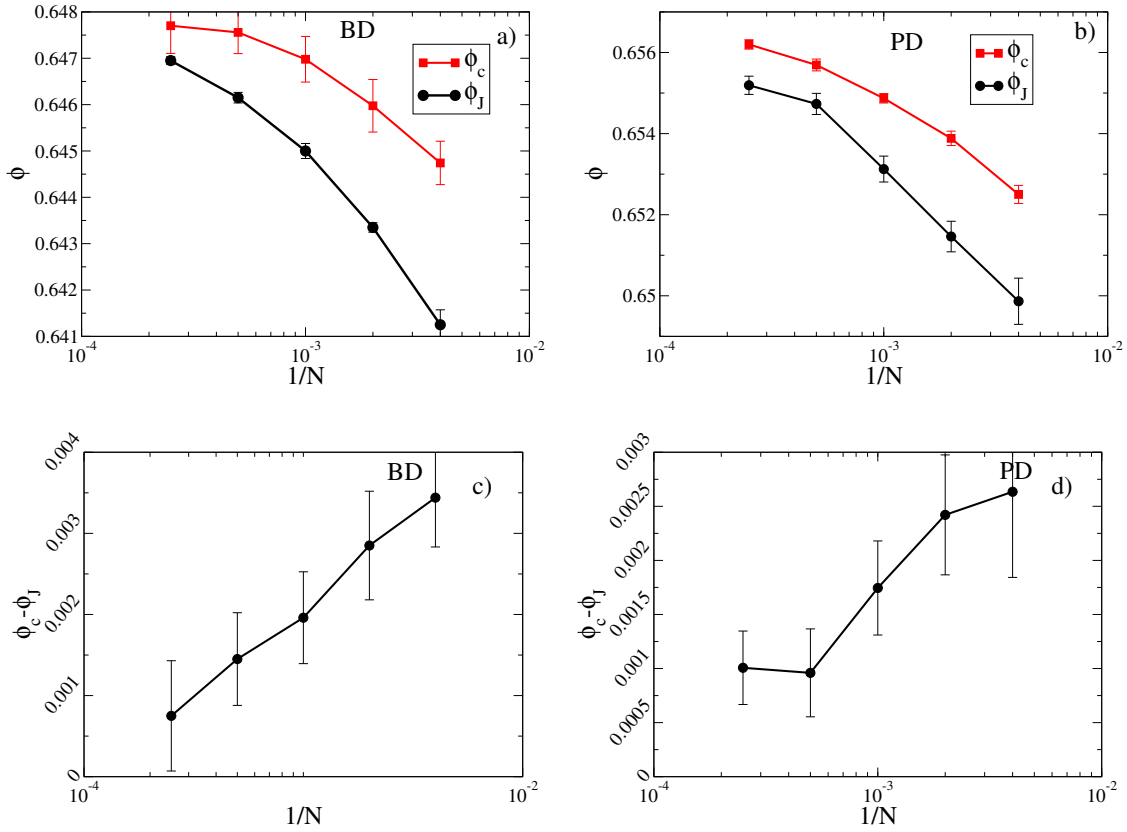

FIG. S6. **Finite size analysis of ϕ_J and ϕ_c for the BD and PD model. a) and b)** Densities ϕ_J and ϕ_c as functions of $1/N$. **c) and d)** The difference $\phi_c - \phi_J$ is plotted as a function of $1/N$. The error bars represent standard errors.

After that, we minimize the energy of the system using the FIRE algorithm [1]. If the system is jammed (the residual potential energy per particle after minimization is larger than 10^{-16}), we decrease $\delta\phi$ by a factor of 2 and decompress the system until it becomes unjammed. We perform a series of decompression and compression as described above, until $\delta\phi < 10^{-6}$. Lastly, we perform an additional cycle of compression and decompression: the compression is performed with $\delta\phi = 10^{-5}$ until the residual energy per particle is larger than 10^{-6}, and the decompression is performed with $\delta\phi = 10^{-6}$ until the system becomes unjammed. We identify this unjamming density as ϕ_J.

To estimate the critical state density ϕ_c, we perform constant pressure AQS at a few different P_s, by minimizing the enthalpy using the FIRE algorithm, and measure the volume fraction $\phi_s(P_s)$ when the stress reaches a constant value. Then we extrapolate ϕ_c from $\phi_s(P_s)$ using the linear relation near the zero pressure limit.

The system size dependence of ϕ_J and ϕ_c are shown in FIG. S6 a) and b), and the difference $\phi_c - \phi_J$ is plotted as a function of the system size N in FIG. S6 c) and d). Our results show that ϕ_c is always slightly larger than ϕ_J in finite size systems, but the difference decreases with N. In this paper, we regard $\phi_J \simeq \phi_c$ in the thermodynamical limit $N \to \infty$. However, note that several previous studies [9–11] in two dimensions suggested that this difference remains finite (around 0.001-0.002), even in the thermodynamical limit. We do not exclude such a possibility in three dimensions based on our data.

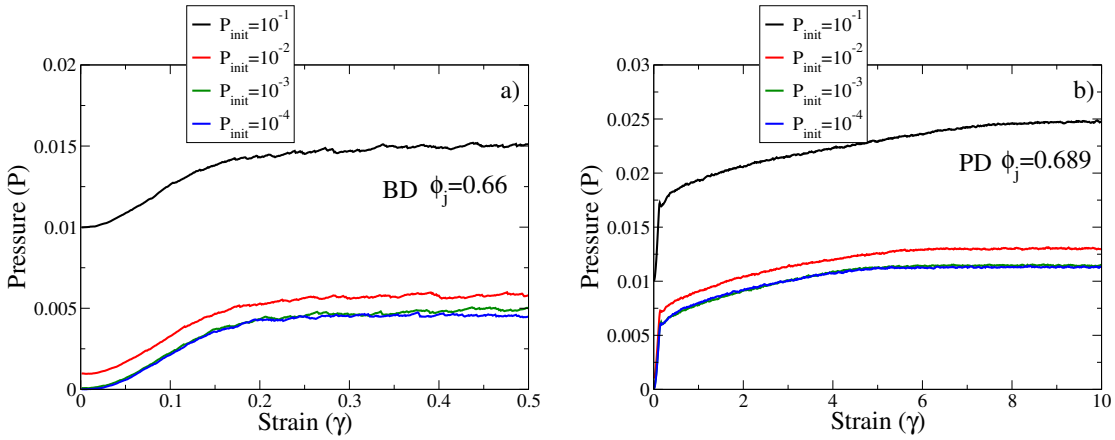

FIG. S7. **Pressure P as a function of strain γ under constant volume shear deformations, for over-compressed systems.** The pressure increases from the initial value P_{init} as the system is strained in both **a)** BD and **b)** PD systems.

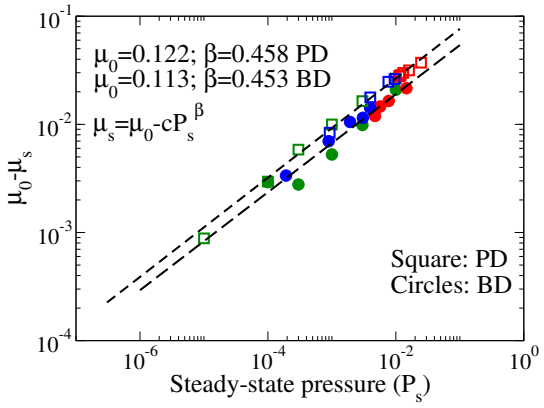

FIG. S8. **Scaling relationship between the steady-state macroscopic friction μ_s and pressure P_s.** The data for both BD ($\phi_j \approx 0.660$) and PD ($\phi_j \approx 0.689$) systems are fitted to the empirical scaling form $\mu_s = \mu_0 - cP_s^\beta$ (dashed lines). The data obtained from constant pressure shear (green), constant volume shear for $\phi_J < \phi < \phi_j$ (shear jamming, blue), and constant volume shear for $\phi > \phi_j$ (red) are presented.

S6. DILATANCY EFFECT REVEALED BY PRESSURE INCREASE UNDER CONSTANT VOLUME SHEAR

For over-compressed systems with a jamming density ϕ_j above ϕ_J, the pressure P increases under constant volume shear deformations, which is an effect equivalent to dilatancy in constant pressure shear. FIG S7 shows how the pressure P increases from P_{init} when the constant volume shear is applied, and FIG S4 shows the evolutions of the macroscopic friction μ. We find that the peak in macroscopic friction is more prominent for configurations with a larger ϕ_j. The scaling relationship between the steady-state macroscopic friction μ_s and pressure P_s, $\mu_s = \mu_0 - cP_s^\beta$, is shown in FIG S8. Note that, in Fig. 1 of the main text and Sec. S3, the initial configurations are unjammed ($P_{init} = 0$ or $\phi < \phi_j$). In that case, the constant volume shear deformation firstly jams the system, and then increases the pressure (see FIG S1).

S7. ADDITIONAL DATA FOR EQUATIONS OF STATE

A. Equations of state of steady-states

Here we explain how to obtain the steady-state equations of state (EOSs) of pressure $P_s(\phi_s)$ and of stress $\sigma_{xz,s}(\phi_s)$. For the EOS of pressure, we firstly calculate the average pressure-strain curve $P(\gamma) = \langle P^{ind}(\gamma)\rangle$ in constant volume shear simulations where the density $\phi = \phi_s$ is fixed, or the average density-strain curve $\phi(\gamma) = \langle \phi^{ind}(\gamma)\rangle$ in constant pressure shear simulations where the pressure $P = P_s$ is fixed. Here $P^{ind}(\gamma)$ and $\phi^{ind}(\gamma)$ are the pressure and density of individual samples at strain γ, and $\langle \ldots \rangle$ represents the sample average. We then extrapolate the large-γ limits of $P(\gamma)$ and $\phi(\gamma)$ as the steady-state values P_s and ϕ_s. By varying the control parameter ϕ_s in constant volume shear, and P_s in constant pressure shear, we obtain the pressure EOS $P_s(\phi_s)$ for both protocols (FIG S9). The same procedure is applied to get the stress EOS $\sigma_{xz,s}(\phi_s)$.

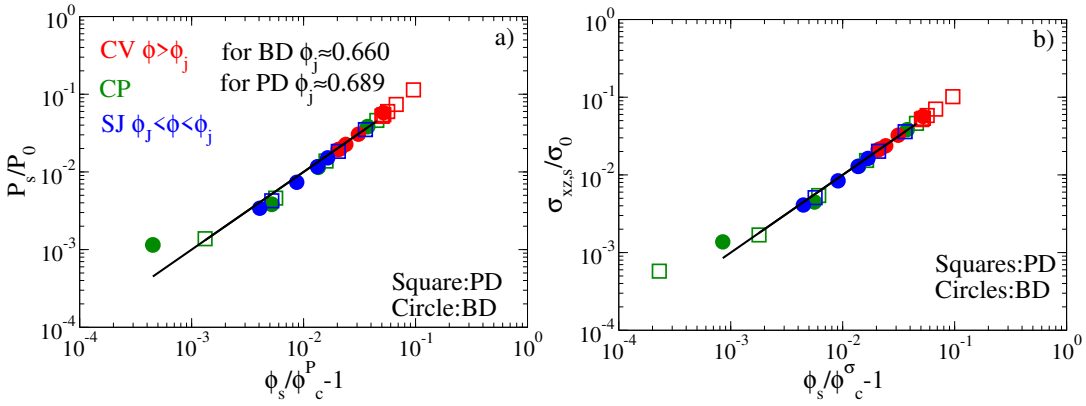

FIG. S9. **Critical scalings of steady-states.** We fit the EOS data of (a) pressure and (b) stress to Eqs. (S3) and (S4). The fittings are represented by solid lines.

TABLE S1. Values of fitting parameters in Eqs. (S3), (S4), and (S5), for both BD ($\phi_j = 0.660$) and PD ($\phi_j = 0.689$) models. The steady-state data, P_0, ϕ_c^P, σ_0 and ϕ_c^σ, are obtained from constant pressure shear; the constant volume shear gives the same results because the EOSs are independent of shear protocols (see FIG S9).

	P_0	ϕ_c^P	σ_0	ϕ_c^σ	P_0'	ϕ_J
BD	0.261	0.647	0.024	0.647	0.29	0.648
PD	0.217	0.656	0.021	0.656	0.21	0.655

To estimate the density ϕ_c of the critical state, we fit the EOS data $P_s(\phi_s)$ and $\sigma_{xz,s}(\phi_s)$ to the asymptotic linear scalings near the zero pressure limit,

$$P_s(\phi_s) = P_0(\phi_s/\phi_c^P - 1), \tag{S3}$$

and

$$\sigma_{xz,s}(\phi_s) = \sigma_0(\phi_s/\phi_c^\sigma - 1), \tag{S4}$$

where $P_0, \sigma_0, \phi_c^P, \phi_c^\sigma$ are fitting parameters (see FIG S9). The values of the fitting parameters are summarized in TABLE S1, which show that consistently $\phi_c^P = \phi_c^\sigma$ within the numerical uncertainty. We therefore determine the critical-state density as $\phi_c = \phi_c^P = \phi_c^\sigma$.

B. Equation of state of isotropic-jamming

We first measure the pressure $P_{iso}^{ind}(\Delta\phi)$ at a given $\Delta\phi = \phi - \phi_J^{ind}$ for each individual sample, where ϕ_J^{ind} is the individual sample jamming density determined according to the jamming criterion described in METHODS. To do

that, we compress the configuration from ϕ_J^{ind} in small increments of density $\delta\phi = 10^{-4}$, up to the target density $\phi > \phi_J^{ind}$. We then average over samples to obtain the EOS, $P_{iso}(\Delta\phi) = \langle P_{iso}^{ind}(\Delta\phi)\rangle$. The isotropic jamming density ϕ_J is determined from the average value of ϕ_J^{ind}, $\phi_J = \langle\phi_J^{ind}\rangle$. The isotropic jamming EOS satisfies the linear scaling near ϕ_J,

$$P_{iso}(\phi) = P_0'(\phi/\phi_J - 1), \tag{S5}$$

where $P_0' = 0.29$ (BD model) and 0.21 (PD model) are used to re-scale P_{iso} such that the isotropic jamming and the steady-sate EOSs collapse onto the universal curve (Fig. 3a). The values of ϕ_J and P_0' are listed in TABLE S1.

S8. ADDITIONAL DATA FOR THE GENERALIZED ZERO-TEMPERATURE JAMMING PHASE DIAGRAM

In FIG S10 we show the generalized zero-temperature jamming phase diagram for the BD model. Similar to the PD case (Fig. 4), the yield stress shows a discontinuous jump at ϕ_j for $\phi_j > \phi_J$. This behavior is independent of the definition of the yield stress, which can be seen from Fig. 4 where σ_Y is defined as the steady-state value σ_s, and from FIG S11 where σ'_Y is defined as the peak value of the shear stress in the stress-strain curve (both figures are for the PD model).

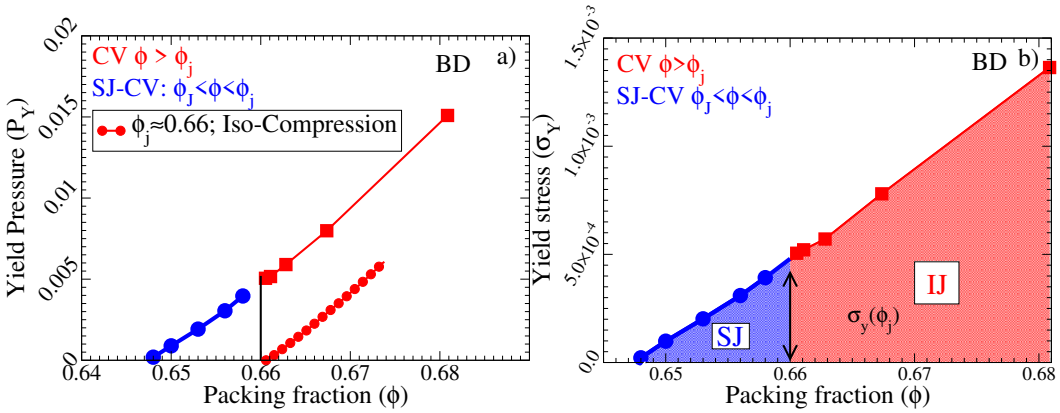

FIG. S10. **Generalized zero-temperature jamming phase diagram for the BD model. a)** Yield pressure ($P_Y = P_s$) as a function of packing density ϕ, obtained by constant volume shear deformations for both $\phi > \phi_j = 0.66$ (isotropic jamming, IJ) and $\phi < \phi_j$ (shear jamming, SJ). The isotropic compression pressure $P_{\rm iso}$ is also plotted. **b)** Yield stress ($\sigma_Y = \sigma_{xz,s}$) as a function of ϕ.

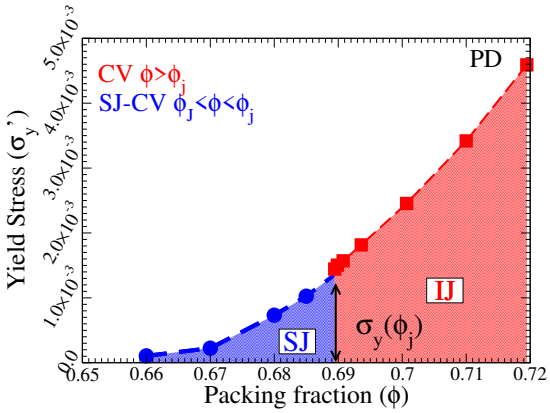

FIG. S11. **Generalized zero-temperature jamming phase diagram for the PD model, where the yield stress σ'_Y is defined as the peak value of the shear stress in the stress-strain curve.** The jamming density is $\phi_j = 0.689$.

S9. JAMMING DENSITIES OF MECHANICALLY ANNEALED BI-DISPERSE SPHERE PACKINGS

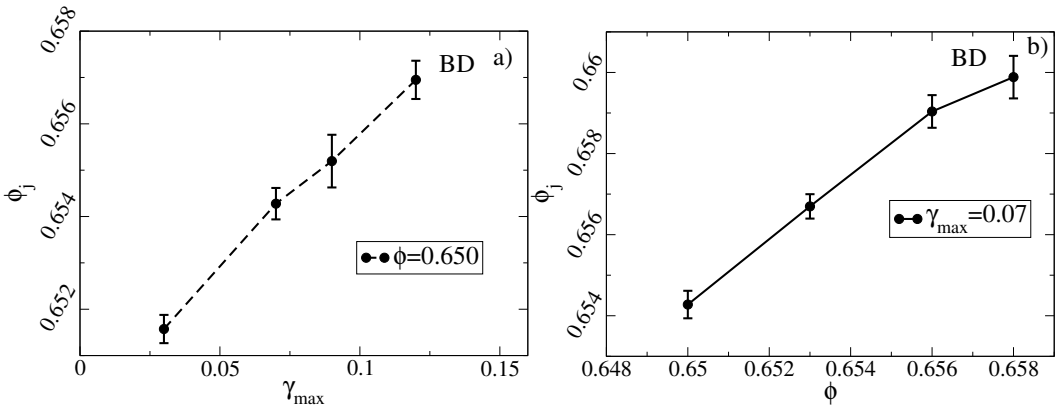

FIG. S12. **Dependence of jamming density ϕ_j on protocol parameters of cyclic AQS, for the BD model. a)** Dependence of jamming density ϕ_j on the strain amplitude γ_{max}, for a fixed unjamming density $\phi = 0.650$. **b)** Dependence of jamming density ϕ_j on the unjamming density ϕ, for a fixed $\gamma_{max} = 0.07$. Error bars represent standard deviations.

An over-jammed BD system at packing density ϕ (compressed from $\phi_J \simeq 0.648$), unjams under constant volume cyclic AQS, and jams again at ϕ_j ($\phi_j > \phi > \phi_J$) upon a further compression. The jamming density ϕ_j depends on both the unjamming density ϕ and the strain amplitude γ_{max} of the cyclic shear. As shown in the FIG S12, ϕ_j increases with γ_{max} for a fixed ϕ, and increases with ϕ for a fixed γ_{max}. In the main text, we use $\gamma_{max} = 0.07$, because for this amplitude, the largest range of densities over which unjamming occurs is obtained [4].

S10. PROPOSAL FOR EXPERIMENTAL VALIDATION

We propose to test the following procedure in experiments. The procedure was used in simulations of the BD system in this study, and is expected to be reproducible in shear experiments of colloidal suspensions [12–14] and emulsions [15]. Indeed, non-Brownian suspensions and emulsions have been experimentally investigated in contexts related to our present work in the past.

1. Jamming by compression. Compress an initially unjammed system to an over-jamming density ϕ above ϕ_J.

2. Unjamming by cyclic shear. Keeping the density as a constant at ϕ, after a sufficient number of shear cycles, the system should unjam. Equivalently, the jamming density ϕ_j is uplifted from ϕ_J to some value above ϕ.

3. Jamming by shear. Shear jamming is expected if uniform shear is applied under the constant volume condition (keeping ϕ unchanged) to the unjammed system obtained from (2).

4. Dilatancy under shear. Compress the unjammed system obtained from (2), until it jams again at a higher volume fraction ϕ', where $\phi' > \phi_j > \phi > \phi_J$. The dilatancy effect is expected if uniform shear is applied to this over-jammed system under the constant pressure condition (the pressure is finite since the system is over-jammed).

In many experimental systems, friction is not negligible. It is known that the J-point density $\phi_J(\mu)$ decreases with the inter-particle friction coefficient μ [16]. However, we expect that the above procedure will result in shear jamming and dilatancy above $\phi_J(\mu)$ even $\mu > 0$. In other words, the jamming density $\phi_J(\mu)$ should be shifted to a higher value $\phi_j > \phi_J(\mu)$ under cyclic shear, for any given μ. In fact, a very recent study of a 2D frictional system reported simulation results showing that the jamming density increases with the strain amplitude of athermal cyclic shear (see Fig. 10 of [17]), similar to our data obtained in the 3D frictionless systems (see Fig. S12a). Therefore, shear jamming above the minimum jamming density $\phi_J(\mu)$ is observable in 2D frictional packings as well (see the phase diagram Fig. 8 of [17]), although the effect seems to be subtler compared to the case of 3D frictionless packings (see the phase

diagram Fig. 5 of [4]). In short, we expect that the procedure proposed in this manuscript should in principle work in experimental systems even when friction is non-negligible.

[1] Steve Plimpton, "Fast parallel algorithms for short-range molecular dynamics," Journal of computational physics **117**, 1–19 (1995).

[2] Erik Bitzek, Pekka Koskinen, Franz Gähler, Michael Moseler, and Peter Gumbsch, "Structural relaxation made simple," Physical review letters **97**, 170201 (2006).

[3] Pinaki Chaudhuri, Ludovic Berthier, and Srikanth Sastry, "Jamming transitions in amorphous packings of frictionless spheres occur over a continuous range of volume fractions," Physical review letters **104**, 165701 (2010).

[4] Pallabi Das, HA Vinutha, and Srikanth Sastry, "Unified phase diagram of reversible–irreversible, jamming, and yielding transitions in cyclically sheared soft-sphere packings," Proceedings of the National Academy of Sciences **117**, 10203–10209 (2020).

[5] Ludovic Berthier, Daniele Coslovich, Andrea Ninarello, and Misaki Ozawa, "Equilibrium sampling of hard spheres up to the jamming density and beyond," Phys. Rev. Lett. **116**, 238002 (2016).

[6] Ludovic Berthier, Patrick Charbonneau, Yuliang Jin, Giorgio Parisi, Beatriz Seoane, and Francesco Zamponi, "Growing timescales and lengthscales characterizing vibrations of amorphous solids," Proceedings of the National Academy of Sciences **113**, 8397–8401 (2016).

[7] Corey S O'Hern, Leonardo E Silbert, Andrea J Liu, and Sidney R Nagel, "Jamming at zero temperature and zero applied stress: The epitome of disorder," Physical Review E **68**, 011306 (2003).

[8] Daniele Coslovich, Ludovic Berthier, and Misaki Ozawa, "Exploring the jamming transition over a wide range of critical densities," SciPost Physics **3**, 027 (2017).

[9] Claus Heussinger, Pinaki Chaudhuri, and Jean-Louis Barrat, "Fluctuations and correlations during the shear flow of elastic particles near the jamming transition," Soft matter **6**, 3050–3058 (2010).

[10] Wen Zheng, Shiyun Zhang, and Ning Xu, "Jamming of packings of frictionless particles with and without shear," Chinese Physics B **27**, 066102 (2018).

[11] Daniel Vågberg, Peter Olsson, and Stephen Teitel, "Glassiness, rigidity, and jamming of frictionless soft core disks," Physical Review E **83**, 031307 (2011).

[12] Nathan C. Keim and Paulo E. Arratia, "Mechanical and microscopic properties of the reversible plastic regime in a 2d jammed material," Physical Review Letters **112**, 028302 (2014).

[13] K. Hima Nagamanasa, Shreyas Gokhale, A K Sood, and Rajesh Ganapathy, "Experimental signatures of a nonequilibrium phase transition governing the yielding of a soft glass," Physical Review E **89**, 062308 (2014).

[14] David J Pine, Jerry P Gollub, John F Brady, and Alexander M Leshansky, "Chaos and threshold for irreversibility in sheared suspensions," Nature **438**, 997–1000 (2005).

[15] M. Clusel, E. Corwin, A. Siemens, and J. Brujic, "A 'granocentric' model for random packing of jammed emulsions," Nature **460**, 611–615 (2009).

[16] Chaoming Song, Ping Wang, and Hernan A. Makse, "A phase diagram for jammed matter," Nature **453**, 629–32 (2008).

[17] Michio Otsuki and Hisao Hayakawa, "Shear jamming, discontinuous shear thickening, and fragile states in dry granular materials under oscillatory shear," Physical Review E **101**, 032905 (2020).